Advances in Modeling of Aft-Emitted Tonal Noise from a Ducted Fan

Dimitri Papamoschou *
University of California, Irvine, CA, 92697-3975, USA

The paper presents advances in low-cost modeling of aft-emitted tonal fan noise in isolated and installed configurations. The theoretical development is done jointly with experimental measurements in an anechoic facility. The model comprises linear coherent waveforms prescribed on a cylindrical surface downstream of the fan exit. A generic shape for the waveform is proposed based on a simple analytical treatment of the sound field radiated from the fan duct. The waveforms possess the same azimuthal orders as the aft-propagating duct modes that are cut-on. In addition, the initial axial wavenumber, at the duct exit, matches closely that of the internal acoustic field. Downstream of the fan exit the axial wavenumber increases until the propagation speed equals the speed of sound. The shapes of the waveforms are parameterized and the parameter vector is determined by least-squares minimization of the difference between the modeled and experimental cross-spectral densities in the far field. In installed arrangements, the emission from the parameterized source is used as the incident field in the computation of scattering using the boundary element method. The experiment utilized a small-scale ducted fan with rotor tip Mach number of 0.59. Microphone measurements with high spatial resolution were enabled by the combination of fixed sensors with one scanning sensor. The recording of a tachometer enabled filtering of the signals into tonal and broadband components, with the focus here on the second harmonic of the blade pass frequency. Integration of a flat plate enabled measurements in a canonical shielded configuration. The model captures the overall directivity of the experimental spectrum and its modification by insertion of the plate.

I. Introduction

The aviation community has set ambitious targets for the development of ultra-quiet subsonic commercial aircraft, encapsulated by NASA's N+2 and N+3 noise goals [1]. Candidate propulsion schemes revolve around the high-bypass turbofan and the open rotor. Attainment of the noise goals requires not only improvements at the component level, but also a systems integration approach for the design of the propulsor and the airframe. A comprehensive review of candidate configurations can be found in Spakovsky [2]. The shielding of engine noise by the airframe has been of particular interest, with efforts addressing fan inlet [3], fan outlet [4], jet [5], and open rotor [6]. The blended wing body (BWB) airplane design has been central to these efforts because its layout is amenable to innovative integration concepts [7].

The development of efficient predictive tools for the emission of the isolated and installed noise source is critical for the design of these advanced aircraft. In this study, the focus is on aft-emitted fan tonal noise. Even though the problem can be addressed using sophisticated computational techniques (for example, Refs. [8–10]), there is desirability of low-cost models that can provide rapid turnaround with sufficient accuracy. Once a reliable source model is developed, the scattering of the emitted sound can be predicted using techniques such as the boundary element method [11, 12] or the equivalent-source method [13].

This paper presents some advances in the development of a surface-based source model for the aft-emitted fan tonal noise that is informed by key features of the internal pressure field. It builds on an earlier effort presented in Ref. [14]. The primary purpose of the model is prediction of the installed emission given knowledge of the isolated acoustics. The model is developed with the aid of experimental measurements of the noise emitted by a small-scale ducted fan. The experiment featured a phased array that comprised fixed and continuously-scanning sensors. The continuous-scan approach [15–17] in the measurement of the acoustic field provides fine spatial resolution needed in the model development. The model emission is integrated with the BEM to provide scattering predictions for canonical installed configurations.

---

*Professor, Department of Mechanical and Aerospace Engineering, Fellow AIAA.

II. Experimental Details

A. Ducted Fan Setup

At the UCI Aeroacoustics Laboratory, a small-scale ducted fan simulated the fan noise emission of a high-bypass turbofan engine. The ducted fan rig is shown in Fig. 1a, and its detailed design has been documented in Ref. [18]. The nacelle has inlet diameter of 70 mm and exit-to-inlet area ratio of 0.56. The fan outlet diameter is D_o=74 mm. The overall design is based on the GE R4 fan with a rotor blade count of 14 and stator vane count of 24. The design includes a pylon and bifurcation as in a typical turbofan engine. Powered by a 6-hp DC brushless motor, the fan develops a pressure ratio FPR = 1.15 and tip Mach number of 0.59 when it rotates at 55500 RPM. This rotational speed was held to within ~1% in the experiments described here. The exit flow Mach number was $M = 0.45$, and it is assumed that the flow inside the duct near the exit was at approximately the same Mach number. In the installed configuration, Fig. 1b, a rectangular flat plate with span of 610 mm, chord length of 305 mm, and thickness of 3.2 mm was placed near the fan. The plate was located at a height of 65 mm from the fan centerline and its trailing edge was positioned at $X_{TE} = 33$, 55 and 78 mm from the fan exit plane ($X_{TE}/D_o = 0.45$, 0.74 and 1.05, respectively). These positions will be referred to a short, medium, and long shields. Figure 3 illustrates the latter two.
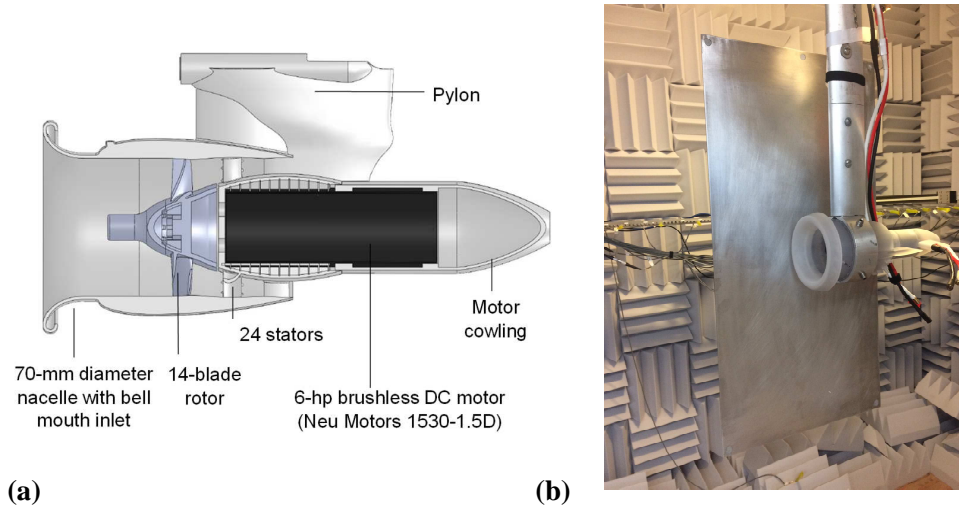

(a)　　　　　　　　　　　　　　　**(b)**

Fig. 1　Small-scale ducted fan rig. (a) Schematic; (b) installation with plate.

B. Diagnostics

Acoustic measurements were performed in the anechoic chamber depicted in Fig. 2 using 23 fixed and one continuously-scanning Bruel & Kjaer Type 4138 microphones, with frequency response up to 120 kHz. The polar angle θ is defined relative to the downstream axis and the distance of the sensors R is measured from the center of the fan exit plane. All the fixed microphones were mounted on a linear inclined holder and covered the polar aperture $26° \leq \theta \leq 121°$. The scanning microphone traversed along the line of the fixed sensors with a lateral offset of 6 mm. Its polar aperture was $32° \leq \theta \leq 73°$. The non-dimensional sensor distance R/D_o ranged from 12.3 to 20.3.

The microphones were sampled simultaneously at a rate of 250 kS/s per channel by six National Instruments PCI-6143 data acquisition boards installed in a desktop computer. The scan speed was 76.2 mm/s and the experimental duration was 12 s over which 3000000 samples were acquired. Positioning of the scanning microphone was determined from the encoder signal of the motor powering the traverse and was verified by a laser displacement sensor. Details of the scanning setup can be found in Refs. [16, 17]. In addition to the microphones, a tachometer measured the rotational speed of the rotor and Pitot probes measured the total pressure at the fan exit.
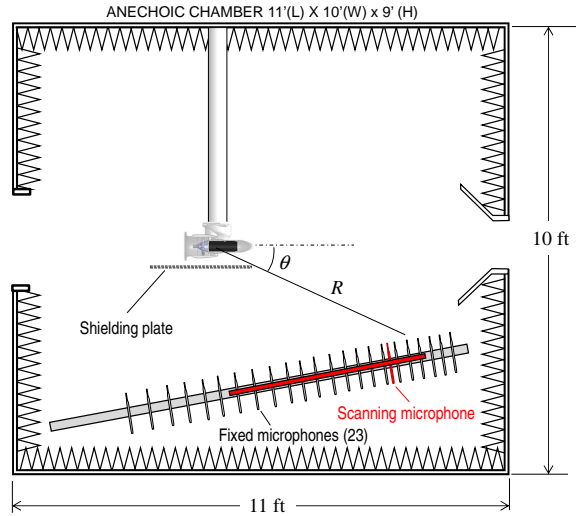
Fig. 2   Anechoic chamber setup.

C. Signal Processing

Spectral densities were computed with Fast Fourier Transform (FFT) size of 2048, yielding a frequency resolution of 122 Hz. Sound pressure level (SPL) spectra, at polar angle $\theta = 49.4°$ are plotted in Fig. 3 for the isolated and shielded configurations. The fundamental blade passing frequency (BPF) was near 13.0 kHz. Tones up to the sixth harmonic are evident in the plots. It is notable that the plate reduces broadband noise significantly, but not all the tonal levels. For certain polar-angle ranges some tones actually amplify.
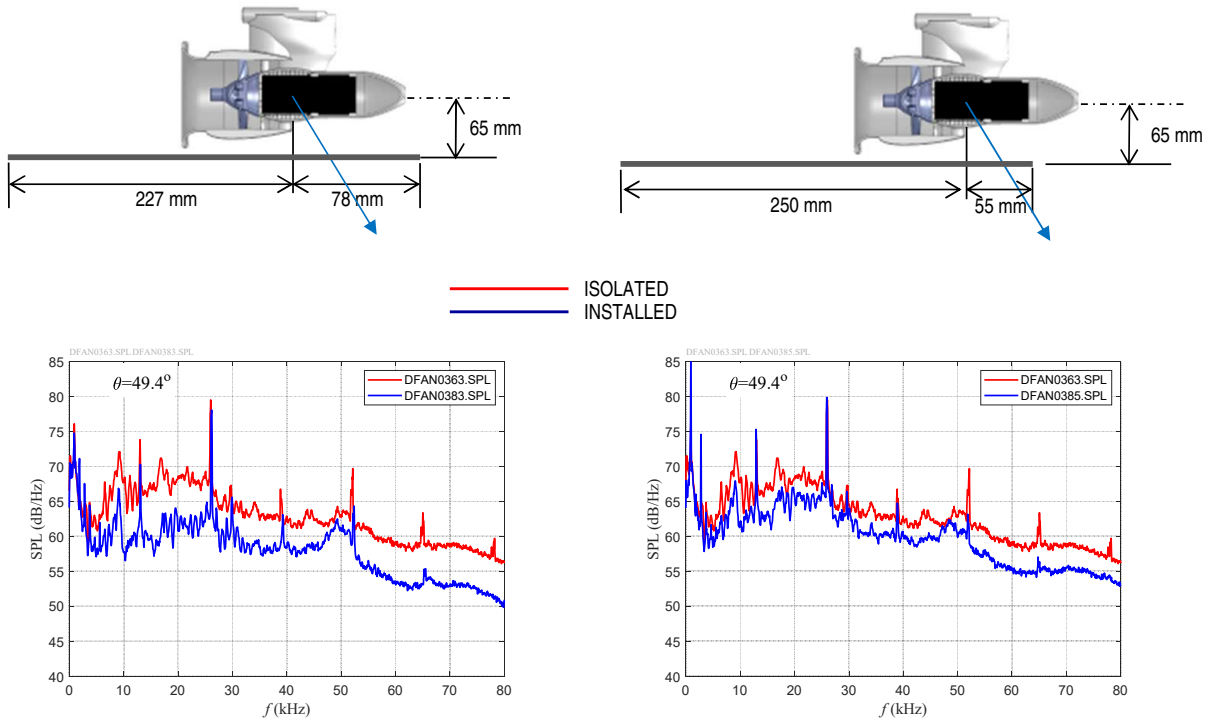
Fig. 3   Narrowband SPL spectra at polar angle $\theta = 49.4°$ for the isolated and installed configurations at two shield lengths.

3

The focus of this project being on tonal noise, the Vold-Kalman filter [19–21] was used to separate the tonal (harmonic) and broadband content, aided by the tachometer measurement. A typical separation is presented in Fig. 4. The power spectral density (PSD) of each harmonic is defined as the integral of the harmonic spectrum centered around the tone frequency (that is, the area under a given spike). Similarly, the cross-spectral density (CSD) of each harmonic is the integral of the harmonic part of the cross-spectrum centered at the tone frequency.
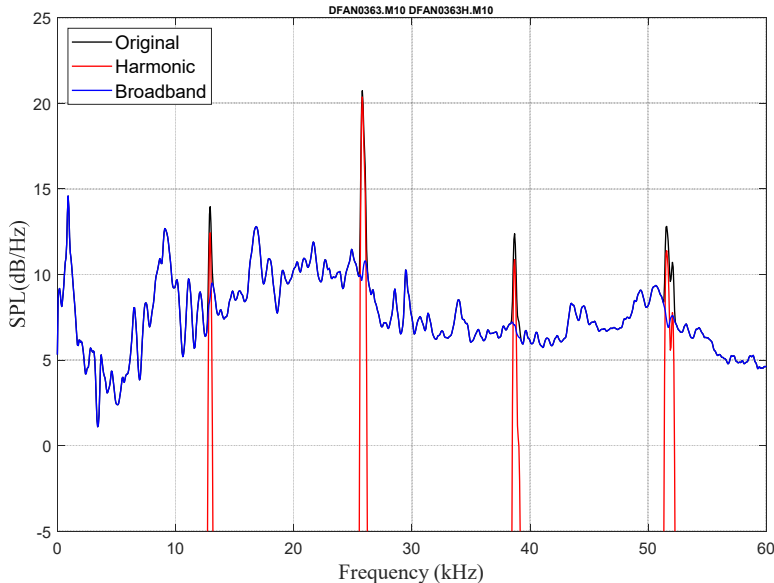
Fig. 4   Example of Vold-Kalman filtering: spectral densities of original signal and its harmonic and broadband components.

Use of the scanning microphone requires division of the signals into a number of relatively short blocks, then correlating the fixed and scanning microphone signals for each block [17]. Here 70 blocks were used, each containing 131072 samples, with overlap of 67%. When computing the tone amplitude for each block, it was noted that the amplitude varied substantially from block to block (i.e., with time). To mitigate this effect the harmonic signal was detrended by dividing it by the short-time (10-ms window) rms and multiplying it by the long-time (2s-window) rms. Beamforming using the Bayesian coherence-based estimation technique of [22] was performed for two array apertures, one covering low polar angles and the other covering high polar angles. Imaging at low polar angle showed only one source location near the fan exit plane. The image at large polar angle showed also a distinct contribution from the fan inlet. Given that the focus of this project is aft tonal emission, the polar angle range of interest was confined to less than 75° to minimize the influence of the inlet.
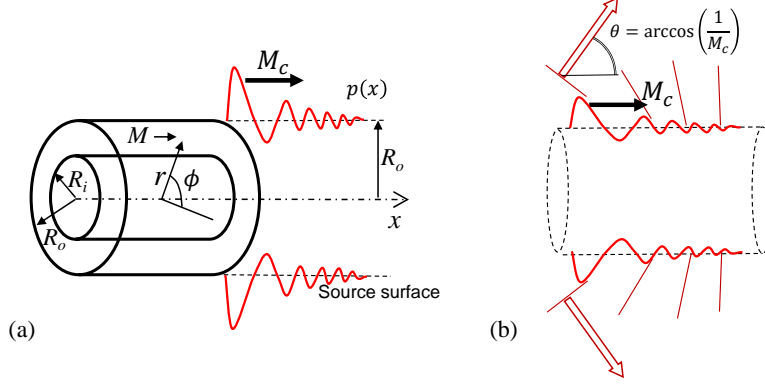
III. Model for Aft Tonal Emission

A. Fundamentals

The noise source model for aft tonal emission is defined as a collection of coherent waveforms prescribed on a near-field surface, as drawn in Fig. 5a. This concept is inspired by earlier efforts to model the jet noise source and its diffraction [11, 23], the difference here being that the tonal noise is deterministic (versus the randomness of the jet turbulence). The polar coordinate system (x, r, ϕ) is used as shown in Fig. 5(a), with x referenced to the fan exit plane. The source surface is a circular cylinder with radius $r = R_o$, where R_o is the outer radius of the fan duct at the exit plane. A central assumption in the model is that the waveforms retain key characteristics of the sound propagation inside the duct.

An earlier effort considered waveforms with constant convective velocity (constant axial wavenumber) modulated by an amplification-decay envelope [14], thus reminiscent of the wavepacket model for jet noise [23]. Further investigation of the physics of aft-noise emission motivated a re-examination of that model and formulation of a different type of waveform. This development is presented here. For both the past and present efforts, the waveforms retain certain

4

elements of the duct acoustics field. Therefore a brief discussion of the internal acoustics is offered first.

Fig. 5   (a) Surface-based source model for aft tonal emission; (b) illustration of Mach wave radiation.

B. Internal Pressure Field

The relations for the internal pressure field follow those in Redonnet and Druon [9]. Consider an annular duct with outer radius R_o, inner radius R_i, and uniform mean Mach number M, as shown in Fig. 5a. The solution of the wave equation inside the duct at radian frequency ω gives the aft-propagating pressure field

$$p_{in}(x, r, \phi, t) \ = \ \sum_{m=-\infty}^{\infty} \sum_{n=0}^{\infty} C_{mn} D_{mn}(k_{r_{mn}} r) e^{i(k_{x_{mn}} x + m\phi - \omega t)} \tag{1}$$

The symbols m and n denote the azimuthal and radial orders, respectively. The total field is a sum of modes, each mode defined by the product of the separable radial, axial and azimuthal eigenfunctions: D_{mn}, $e^{ik_{x_{mn}}x}$, and $e^{im\phi}$. The complex coefficient C_{mn} sets the amplitude and phase of each field associated with azimuthal mode number m and radial mode n, where possible values of these integers are indicated in the summation limits. The axial and radial wavenumbers, $k_{x_{mn}}$ and $k_{r_{mn}}$, are constrained by the dispersion relation

$$k_{x_{mn}} \ = \ \frac{k}{1-M^2} \left\{ -M + \sqrt{1 - (1-M^2)\left(\frac{k_{r_{mn}}}{k}\right)^2} \right\} \tag{2}$$

where $k = \omega/a$ is the acoustic wave number and a is the ambient speed of sound. For a given frequency, the value of the radial wavenumber determines whether the axial wavenumber is real or imaginary. It is evident from Eq. 1 that a real $k_{x_{mn}}$ results in a propagating wave while an imaginary $k_{x_{mn}}$ results in exponential decay. Available radial wavenumbers are set by the hardwall boundary condition

$$J'_m(k_{r_{mn}} R_i)\, Y'_m(k_{r_{mn}} R_o) \ - \ J'_m(k_{r_{mn}} R_o)\, Y'_m(k_{r_{mn}} R_i) \ = \ 0 \tag{3}$$

where J'_m and Y'_m are the derivatives of the Bessel functions of the first and second kind, respectively, and of order m.

For a fan with a rotor containing B blades the radian frequency is $\omega = n_{\mathrm{BPF}} B \Omega$ where Ω is the shaft angular velocity and n_{BPF} takes values of positive integers $(1, 2, \ldots)$ and represents the fundamental blade pass tone and higher harmonics. Including the interaction with a row of stators containing V vanes, per the analysis of Tyler and Sofrin [24] azimuthal mode numbers are constrained to be sums of integer combinations of rotor and stator counts, i.e.,

$$m \ = \ n_{\mathrm{BPF}} B + jV \quad , \quad \begin{matrix} n_{\mathrm{BPF}} = 1, 2, \ldots \\ j = \ldots, -2, -1, 0, 1, 2, \ldots \end{matrix} \tag{4}$$

Combining Eqs. 2, 3, and 4, one determines the axial wavenumber for each n_{BPF} and j. Modes (m, n) for which $k_{x_{mn}}$ is real, and thus disturbances propagate, are referred to as cut-on; while modes for which $k_{x_{mn}}$ is imaginary, and thus disturbances decay, are referred to as cut-off. For the cut-on modes, the speed of convection is $U_{c_{mn}} = \omega/k_{x_{mn}}$ and the

convective Mach number is $M_{c_{mn}} = U_{c_{mn}}/a = k/k_{x_{mn}}$ The criterion for sound propagation in the duct is summarized as follows:

$$k_{r_{mn}}\sqrt{1 - M^2} \; < \; k \; : \text{mode is CUT-ON}$$
$$k_{r_{mn}}\sqrt{1 - M^2} \; \geq \; k \; : \text{mode is CUT-OFF} \tag{5}$$

The set of all the cut-on mode will be symbolized as $(m, n) \in G$.

C. The Kirchhoff Approximation

A full analytical treatment of sound radiation from a duct with flow needs to account for the shear layer formed between the exhaust flow and the ambient. The mathematical complexity is significant and the resulting analyses are only applicable to simple canonical configurations [25, 26]. Computational treatments can resolve the interaction of the sound with the shear layer to various degrees of fidelity, but are inherently expensive [8, 27, 28]. Recognizing these challenges, Rice and Saule [29] developed an elegant model for far-field radiation of aft fan noise that relied on earlier models of inlet noise combined with a simple treatment of the refraction through a vortex sheet. Very good agreement with an exact analytical model was demonstrated. However, Rice and Saule's formulation is only valid in the far-field, whereas here we seek a simple model can be used both in the near field and the far field. The early models for inlet noise, found in the works of Tyler and Sofrin [24], Saule [30], and Rice [31], showed satisfactory predictions of the far-field directivity. The foundation of all these models is the Kirchhoff approximation [32], summarized next.
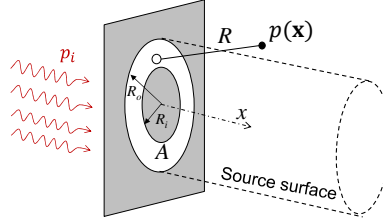
Fig. 6   (a) Illustration of the Kirchhoff approximation for an annular aperture.

Here the Kirchhoff approximation (KA) is used to identify the qualitative features of the near-field sound radiation pattern from a duct without flow, and specifically on a near-field radiator surface from which one can propagate outward. It is surmised that the actual radiation pattern of a realistic duct (with flow) will retain the same qualitative features. These features are then included in a parametric source model.

The KA is connected to Green's third identity. Referring to Fig. 6, consider an infinite opaque screen on the plane $x = 0$ with a cutout defining an aperture with area A. The screen is illuminated on the left ($x \leq 0$) by an incident field p_i. The pressure at a field point $\mathbf{x}$ on the right of the screen ($x > 0$) is given by

$$p(\mathbf{x}) \; = \; \int_A \left[p_i \frac{\partial G}{\partial n} \; - \; G \frac{\partial p_i}{\partial n} \right] d^2\mathbf{y} \tag{6}$$

Here G is the Green's function, $\partial/\partial n$ denotes the normal derivative, and $\mathbf{y}$ is the source coordinate over the aperture. The incident field is the internal pressure field given by Eq. 1. Considering a specific cut-on mode (m, n) at unit amplitude, and suppressing the harmonic term, we have

$$p_i \; = \; D_{mn}(k_{r_{mn}} r)e^{i(k_{x_{mn}} x + m\phi)} \tag{7}$$

and

$$\frac{\partial p_i}{\partial n} \; = \; \frac{\partial p_i}{\partial x} \; = \; ik_{x_{mn}} p_i \tag{8}$$

For a circular aperture,

$$D_{mn}(k_{r_{mn}} r) \; = \; J_m(k_{r_{mn}} r) \tag{9}$$

For an annular aperture,

$$D_{mn}(k_{r_{mn}} r) \; = \; J_m(k_{r_{mn}} r) \; - \; \frac{J'_m(k_{r_{mn}} R_i)}{Y'_m(k_{r_{mn}} R_i)} Y_m(k_{r_{mn}} r) \tag{10}$$

6

The Green's function has the free-space form

$$G = \frac{e^{ikR}}{4\pi R} \ , \quad R = |\mathbf{x} - \mathbf{y}| \tag{11}$$

The integral of Eq. 6 can thus be readily evaluated.

An illustrative example is given next for the exit geometry of the ducted fan detailed in the next section and f=38.8 kHz, which corresponds to $n_{\mathrm{BPF}} = 3$. The cut-on modes for no flow ($M = 0$) include mode (18,1) with $M_c = 1.89$. The pressure field computed using the KA is depicted in Fig. 7. On the line $r = R_o$ and at fixed azimuthal angle, the axial wavenumber k_x is determined from the zero-crossings of the real part of the pressure. The convective Mach number is obtained from $M_c = k/k_x$. The distributions of pressure and M_c on $r = R_o$ are plotted in Fig. 8. It is noted that the amplitude of the pressure starts decaying shortly downstream of the aperture. The convective Mach number starts from a supersonic value close to that predicted by duct acoustics and decays axially as well, tending towards the value of 1.

Assessment of a more realistic geometry for the same exit radii and $n_{\mathrm{BPF}} = 3$ was considered. The annular aperture is followed by a conical cowl of length equal to the outer radius of the aperture and convergence angle (cone half-angle) of 30°. This problem is not amenable to the KA, so the boundary element method (BEM) was utilized using an axisymmetric surface whose cross-section is depicted by the gray outline of Fig. 9. The surface was covered with a triangular mesh and a normal velocity field was prescribed on it. The velocity boundary condition was zero everywhere except over the annular aperture on $x = 0$, on which it took values $v_n = (-i/\omega)\partial p_i/\partial n$, with $\partial p_i/\partial n$ given by Eq. 8. The pressure field computed using the BEM is depicted in Fig. 9, where it is noted that its directivity pattern is different from that of the planar aperture. The distributions of pressure and M_c on $r = R_o$, plotted in Fig. 10, have the same qualitative trends as for the planar aperture but are quantitatively different. Variations of the cowl geometry, including cylindrical and shorter versions, resulted in similar trends but with quantitative differences. This indicates the limited practicality of sophisticated mathematical models that, realistically, can only treat canonical configurations. On the other hand, computational solutions can handle complex geometries but are too expensive as design tools. Here we attempt a mix of theory and empiricism, applying what was learned from this exercise to parametric source model that hopefully contains the essential physics.

The major conclusion of this analysis is that the pressure distribution on the source surface is very different from the jet-inspired wavepacket model used earlier. A new formulation for the noise source is presented in the next section.
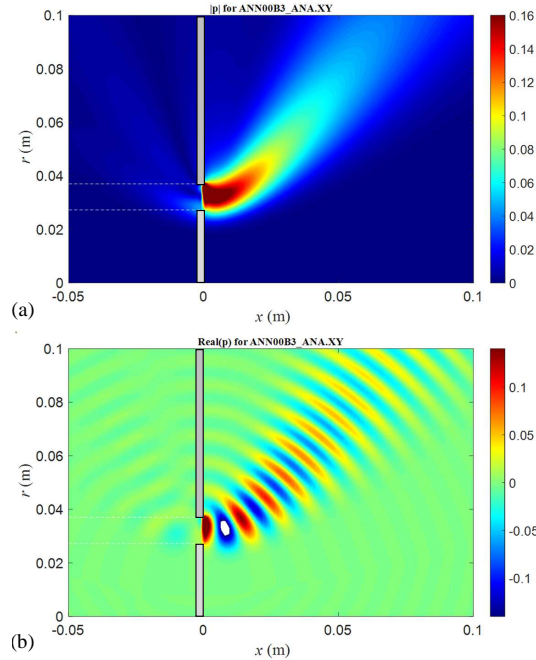

Fig. 7 (a) Pressure field obtained using the Kirchhoff approximation for cut-on mode (18,1) corresponding to $n_{\mathrm{BPF}} = 3$ and zero flow. (a) Magnitude; (b) real part.
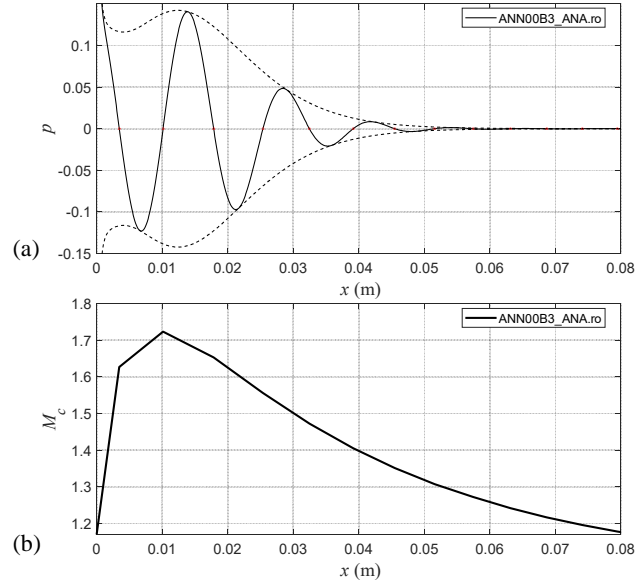
Fig. 8 **(a) Axial distributions on the surface** $r = R_o$ **for the case of Fig. 7. (a) Real part (solid line) and amplitude envelope (dashed line) of pressure; (b) convective Mach number** M_c**.**
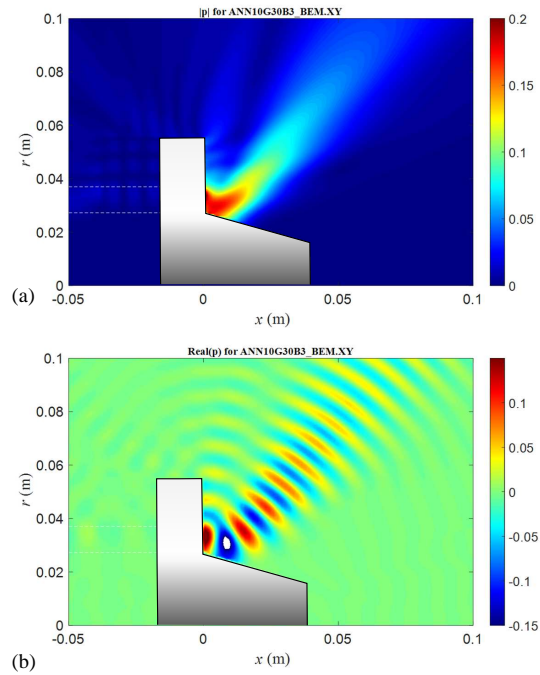
Fig. 9 **(a) Pressure field obtained using the BEM for cut-on mode (18,1) corresponding to** $n_{\mathrm{BPF}} = 3$ **and zero flow. (a) Magnitude; (b) real part. Radial coordinates of BEM surface are included.**
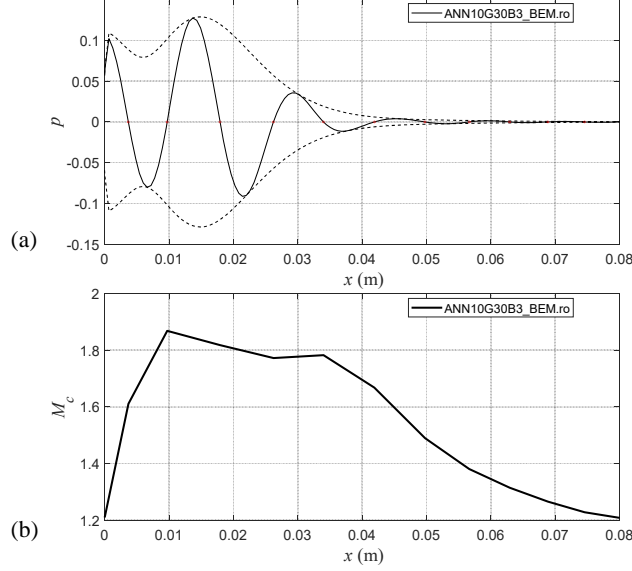
Fig. 10 (a) Axial distributions on the surface $r = R_o$ for the case of Fig. 9. (a) Real part (solid line) and amplitude envelope (dashed line) of pressure; (b) convective Mach number M_c.

D. External Source

In the analysis that follows the harmonic dependence $e^{-i\omega t}$ will be suppressed for brevity. It is assumed that the surface-based source outside the duct comprises waveforms that have the same azimuthal modes m as the cut-on modes inside the duct. In addition, at the duct exit ($x = 0$) the axial wavenumber of the waveforms matches approximately that of the cut-on modes. This is denoted as the initial axial wavenumber $k_{x_{mn}}(0)$. Associated with each waveform is the initial convective Mach number

$$M_{c_{mn}}(0) = \frac{k}{k_{x_{mn}}(0)} \tag{12}$$

In analogy with Mach wave emission in supersonic jets, the convective Mach number can be connected to the direction of polar emission via

$$\theta_{mn} = \arccos\left(\frac{1}{M_{c_{mn}}(0)}\right) \tag{13}$$

The concept is illustrated in Fig. 5(b). Temporarily omitting the subscript mn, each waveform is assigned the shape

$$p(x, \phi) = A\mathcal{D}(x) \exp\left[ik_x(x)x + im\phi\right] \tag{14}$$

where A is a complex amplitude and $\mathcal{D}(x)$ is a decay function that reflects the trends seen in Figs. 8 and 10. The convective Mach number is assumed to decay similarly to the amplitude:

$$M_c(x) = 1 + [M_c(0) - 1]\mathcal{D}(x) \tag{15}$$

and thus approaches the value of 1 with increasing distance from the nozzle exit. The axial wavenumber is then determined from

$$k_x(x) = \frac{k}{M_c(x)} \tag{16}$$

The decay function is selected as

$$\mathcal{D}(x) = \exp\left[-b\left(\frac{x}{R_o}\right)^q\right] \tag{17}$$

where b and q are free parameters. Combining Eqs. 14-17, the axial evolution of a given cut-on mode is defined by the parameter vector

$$\mathbf{v} = [A, M_c(0), b, q]$$

9

Considering mode (m, n), the evolution of the waveform is denoted $p_{mn}(\mathbf{v}_{mn}, x, \phi)$. The surface-based source is the coherent summation of all the waveforms:

$$p_{\text{source}}(\mathbf{V}; x, \phi) = \sum_{(m,n) \in G} p_{mn}(\mathbf{v}_{mn}, x, \phi) \tag{18}$$

where

$$\mathbf{V} = [\mathbf{v}_{mn}], \quad (m, n) \in G \tag{19}$$

is the overall parameter vector. Considering that the amplitude A is complex, the overall parameter vector contains five elements for each mode.

Each waveform p_{mn} is propagated to a field point $\mathbf{x}_i = (x, r, \phi)$ outside the source cylinder. For the cylindrical source surface considered here, the solution to the wave equation gives the emitted pressure field [23]

$$P_{mn}(\mathbf{v}_{mn}, \mathbf{x}_i) = \frac{1}{2\pi} \int_{-\infty}^{\infty} \widehat{p}_{mn}(\mathbf{v}_{mn}, \kappa_x, \phi) \frac{H_m^{(1)}(\kappa_r r)}{H_m^{(1)}(\kappa_r R_o)} e^{i\kappa_x x} d\kappa_x \tag{20}$$

Here κ_x and κ_r are the axial and radial wavenumbers associated with the outward propagation, respectively, and are related to the acoustic wavenumber through $k^2 = \kappa_x^2 + \kappa_r^2$; $\widehat{p}_{mn}$ is the axial Fourier transform of p_{mn}; and $H_m^{(1)}$ is the Hankel function of the first kind of order m. Equation 20 was computed using forward and inverse Fast Fourier Transforms (FFTs) enabling rapid evaluation of P_{mn}. The complete pressure field off the source cylinder is obtained from the superposition

$$p(\mathbf{V}; \mathbf{x}_i) = \sum_{(m,n) \in G} P_{mn}(\mathbf{v}_{mn}; \mathbf{x}_i) \tag{21}$$

The cross-spectral density at field points $\mathbf{x}_i$ and $\mathbf{x}_j$ is

$$G_{ij}(\mathbf{V}) = p(\mathbf{V}; \mathbf{x}_i) \, p^*(\mathbf{V}; \mathbf{x}_j) \tag{22}$$

where * denotes the complex conjugate.

The overall parameter vector is obtained by minimizing the difference between the modeled and experimental cross-spectral densities. In doing so, it is important that the autospectral elements be matched in decibel scale. This is to recover as closely as possible the experimental SPL. A linear scale is problematic in this respect because differences in small amplitudes can be disregarded, while they can be relevant to perceived noise. Of course, the cross-spectral elements cannot be represented in decibel scale, so their treatment is linear. This motivates the following cost function:

$$F(\mathbf{V}) = w \left\| 10 \log_{10} \left(\frac{G_{ii}(\mathbf{V})}{G_{\max}(\mathbf{V})} \right) - 10 \log_{10} \left(\frac{G_{\exp,ii}}{G_{\exp,\max}} \right) \right\| + (1 - w) \left\| \frac{G_{ij}(\mathbf{V})}{G_{\max}(\mathbf{V})} - \frac{G_{\exp,ij}}{G_{\exp,\max}} \right\|_{i \neq j} + \mathcal{P}(\mathbf{V}) \tag{23}$$

The first term on the right hand side represents the matching of the SPL spectra and the second term the matching of the off-diagonal elements of the cross-spectral matrix. The respective weighting factors are w and $(1 - w)$, with $0 \leq w \leq 1$. The operation $|| \cdot ||$ signifies the L2-norm. $G_{\exp,ij}$ is the experimental cross-spectral density, $G_{\max}$ is the maximum value of the modeled autospectral density, and $G_{\exp,\max}$ is the maximum value of the experimental autospectral density. The normalizations in Eq. 14 mean that the modeled and experimental cross-spectral densities are matched (in a least-squares sense) up to a multiplicative constant, the ratio $G_{\max}(\mathbf{V})/G_{\exp,\max}$. The term $\mathcal{P}(\mathbf{V})$ is a penalty function that forces an errant element of the vector to return to within a reasonable range. The bounds for $M_c(0)$ were tight near the theoretical value while those for the other parameters were wide. The weighting factor in Eq. 23 was set to $w = 0.5$. The minimization was done using the conjugate gradient algorithm of Shano and Phua [33].

E. Application to Experiments

The UCI fan rig pictured in Fig. 1 has rotor-stator combination of B=14 and V=24. The duct terminates with an inner radius $R_i = 0.0273$ m and outer radius $R_o = 0.0370$ m. As mentioned in Section II.A, the Mach number inside the duct is approximated as $M = 0.45$. The radius of the source surface is placed at $r = R_o$. Tables 1 land 2 list the cut-on modes and their values of the axial wavenumber, convective Mach number, and emission polar angle for $n_{\text{BPF}} = 2$ and $n_{\text{BPF}} = 3$, respectively. It is noted that there are two cut-on modes for $n_{\text{BPF}} = 2$ and three cut-on modes for $n_{\text{BPF}} = 3$. In the

minimization scheme of Eq. 23, the amplitude of the leading mode is set to unity. Accordingly, the overall parameter vector for $n_{\text{BPF}} = 2$ contains 8 elements while that for $n_{\text{BPF}} = 3$ contains 13 elements.

Table 1. Cut-on modes for $n_{\text{BPF}} = 2$

(m, n)	(4,1)	(4,2)
$k_x(0)$ (m^{-1})	309	179
$M_c(0)$	1.53	2.64
θ (deg)	49.2	67.8

Table 2. Cut-on modes for $n_{\text{BPF}} = 3$

(m, n)	(-6,1)	(-6,2)	(18,1)
$k_x(0)$ (m^{-1})	462	380	246
$M_c(0)$	1.53	1.86	2.87
θ (deg)	49.2	57.4	69.5

Table 3. Parameter vector for $n_{\text{BPF}} = 2$

Mode	A	$M_c(0)$	b	q
(4,1)	1.000 $+i$ 0.000	1.560	0.171	3.336
(4,2)	0.155 $+i$ 0.121	2.507	0.327	2.964

Table 4. Parameter vector for $n_{\text{BPF}} = 3$

| Mode	A	$M_c(0)$	b	q
(18,1)	1.000 $+i$ 0.000	2.983	0.575	2.721
(-6,2)	0.038 $-i$ 0.160	2.024	0.751	1.533
(-6,1)	0.108 $-i$ 0.033	1.572	0.514	1.497

The conjugate-gradient minimization of Eq. 23 allows estimation of the parameter vector **V** and thus the shapes of the waveforms. Tables 3 and 4 display the values of the parameters for $n_{\text{BPF}} = 2$ and 3, respectively. Figure 11 shows results of this parameterization for $n_{\text{BPF}} = 2$. The dominant waveform, denoted by the black line in Fig. 11(a), corresponds to mode (4,1) and has peak radiation at $\theta = 49°$. The waveform corresponding to mode (4,2) is denoted by the blue line of Fig. 11(a). It is much weaker but influences the high polar angles near 65°. Figures 11(b) and (c) compare the experimental and modeled sound pressure level and cross-spectral density, respectively. The spectral results are normalized by the peaks of their respective autospectra. The modeled SPL follows well the directivity of the experimental one, showing a primary peak at $\theta \approx 48°$ and a secondary peak at $\theta \approx 65°$, values in line with the theoretical prediction of Table 1.

The corresponding parameterization results for $n_{\text{BPF}} = 3$ are shown in Fig. 12. Here the dominant waveform, denoted by the black line in Fig. 12(a), corresponds to mode (18,1) and has peak radiation at $\theta = 68°$. The waveforms for modes (-6,1) and (-6,2), denoted by the blue and green lines, are much weaker and influence the low polar angles. All the waveforms are much more compact than for $n_{\text{BPF}} = 2$. Reasonable agreement is noted for the experimental and modeled SPL as well as the corresponding cross-spectral matrices.

The richness of the information enabled by the continuous-scan paradigm is evident in the spectral figures. Without the scanning microphone, the polar resolution would have been about 4°. With the scanning microphone, the polar resolution is approximately 0.5°. It is clear that many features of the cross- and auto-spectra would be missed if only the fixed sensors were used.
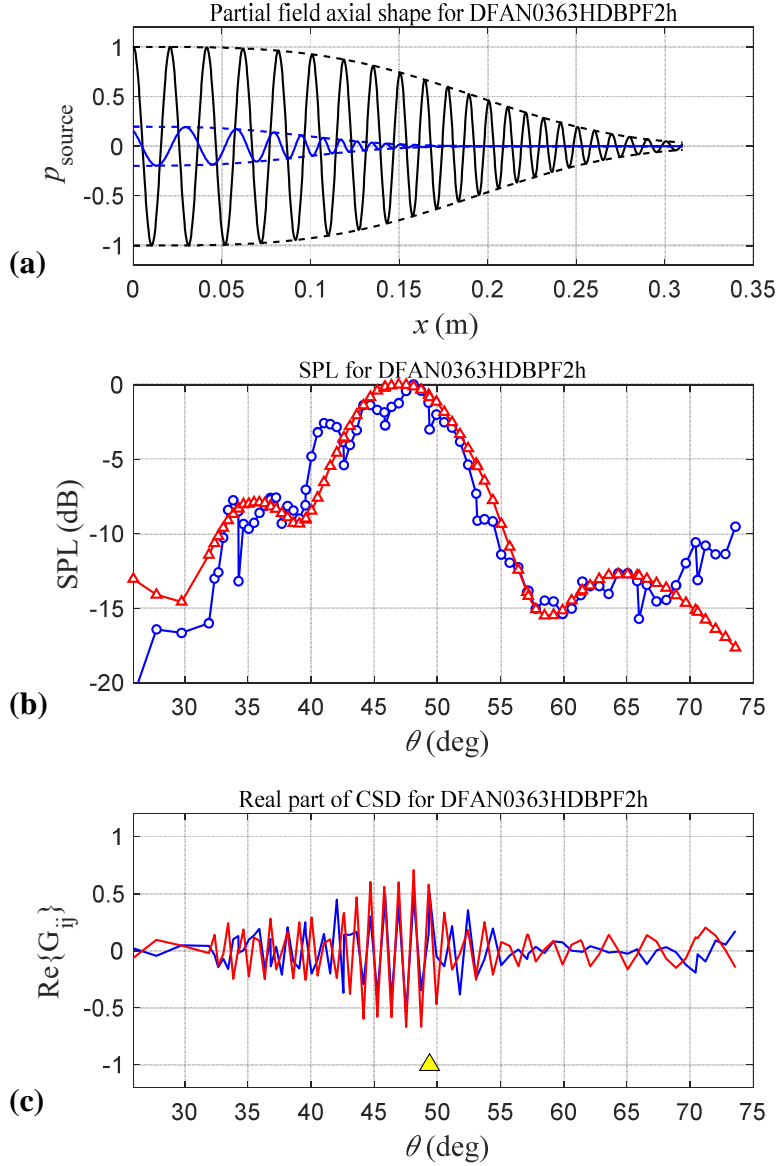
Fig. 11 **Source parameterization based on far-field data for** $n_{\text{BPF}} = 2$. **(a) Waveforms; (b) directivity of SPL for experiment (blue) and model (red); (c) directivity of real part of cross-spectral matrix, with reference sensor at** $\theta = 48°$, **for experiment (blue) and model (red).**
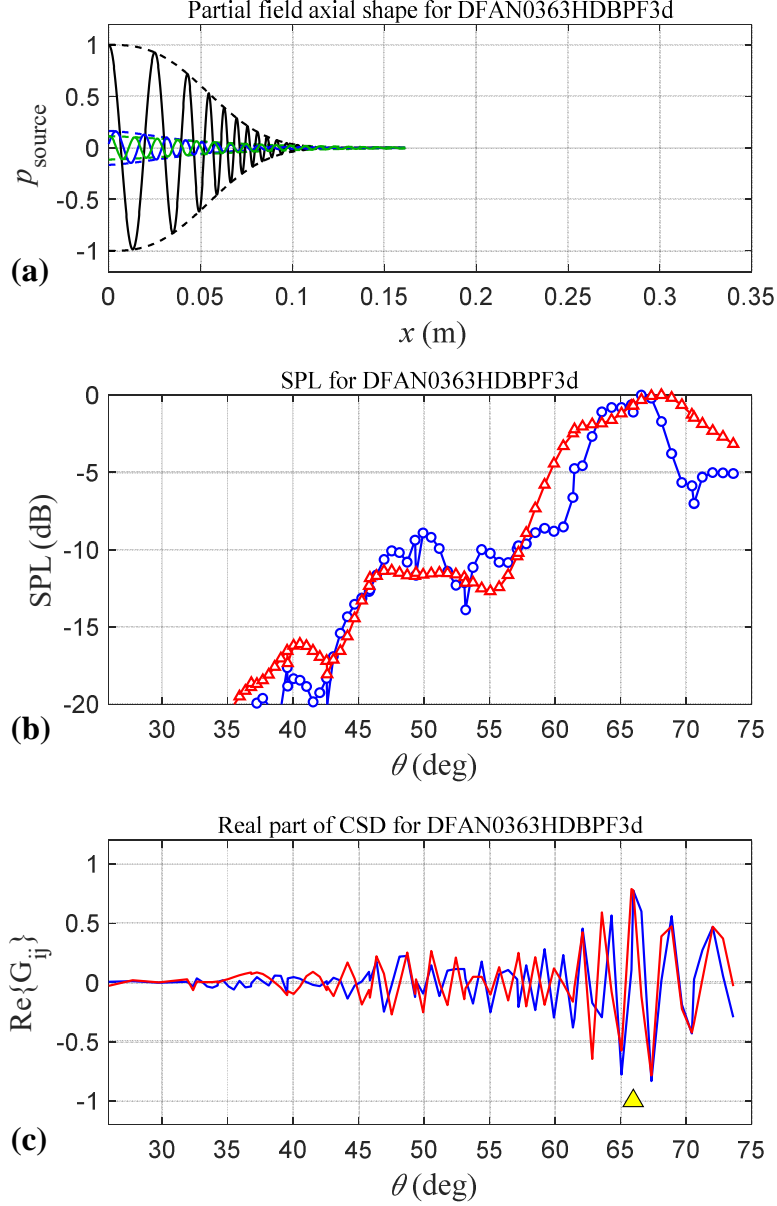
Fig. 12   Source parameterization based on far-field data for $n_{\mathrm{BPF}} = 3$. (a) Waveforms; (b) directivity of SPL for experiment (blue) and model (red); (c) directivity of real part of cross-spectral matrix, with reference sensor at $\theta = 66°$, for experiment (blue) and model (red).

IV. Prediction of Installed Emission

The near-field surface source model generated the incident field for computing the diffraction around the plate installed near the ducted fan. The numerical plate had the same dimensions and placement as the experimental one. The diffraction from the parameterized source was computed using the Fast Multipole BEM [34] (FastBEM software, Advanced CAE Research, LLC). The non-dimensional wavenumber based on chord length c was $kc = 145$ for $n_{\mathrm{BPF}} = 2$ and $kc = 217$ for $n_{\mathrm{BPF}} = 3$. The computation used a triangular mesh with density of four to six elements per wavelength. Meshing was automated and the plate was remeshed for every position of the plate (the coordinate system was always fixed with the fan exit plane). The incident field at the boundary and field points was computed from Eq. 20 using forward and inverse FFTs.

Figure 13 presents contours of the incident and total (incident plus scattered) fields for the isolated and installed

13

pressure fields, the latter with the long shield (X_{TE} = 78 mm). Mach wave emission is evident in all the cases. For n_{BPF} = 2, the shield induces moderate reduction in the amplitude of the downward-emitted sound. For n_{BPF} = 3 a much larger reduction is noted owing to the more compact source and its larger angle of peak emission.
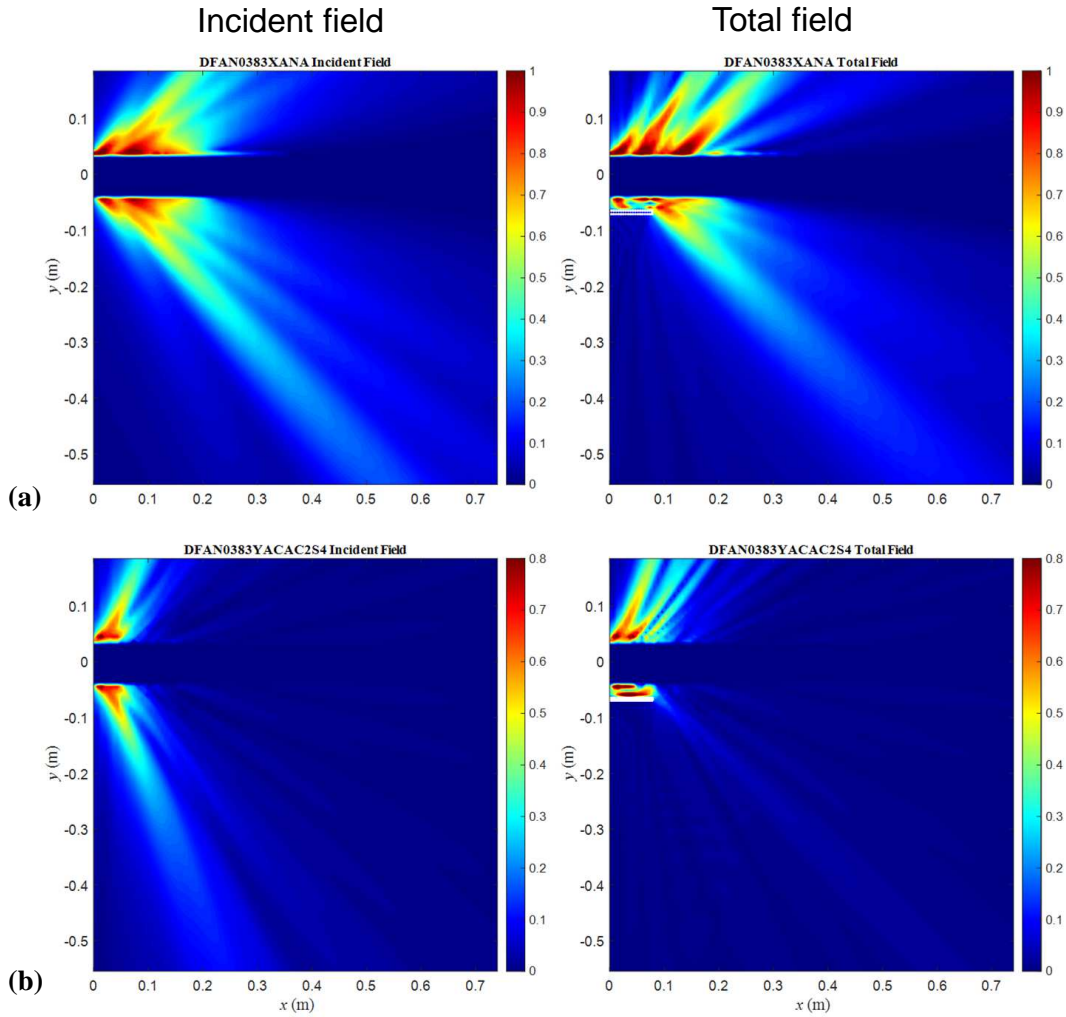

Fig. 13 Magnitude of pressure for incident (left column) and total (right column) fields with long shield. (a) n_{BPF} = 2; (b) n_{BPF} = 3.

Comparisons between the modeled and experimental SPL at n_{BPF} = 2 are shown in Fig. 14 for the three shield lengths. For each set of comparisons, the spectra are normalized by the peak value of the isolated spectrum. For the short shield, both the experiment and the model indicate minimal changes. As the shield elongates, noise reduction becomes appreciable and the overall trends are matched reasonably well by the model. For the long shield the experiment shows SPL reduction of about 2.5 dB at the angle of peak emission θ = 48°, while the model predicts a reduction of about 3.5 dB. The generally modest reductions, even with the long shield length, support the result of Fig. 11(a) of a fairly elongated source.

Analogous results for n_{BPF} = 3 are shown in Fig. 15. Here the shielding are much more pronounced and the model captures well the magnitude and directivity of noise suppression. The larger reductions are consistent with the much shorter source determined through the parameterization process (Fig. 12(a)).
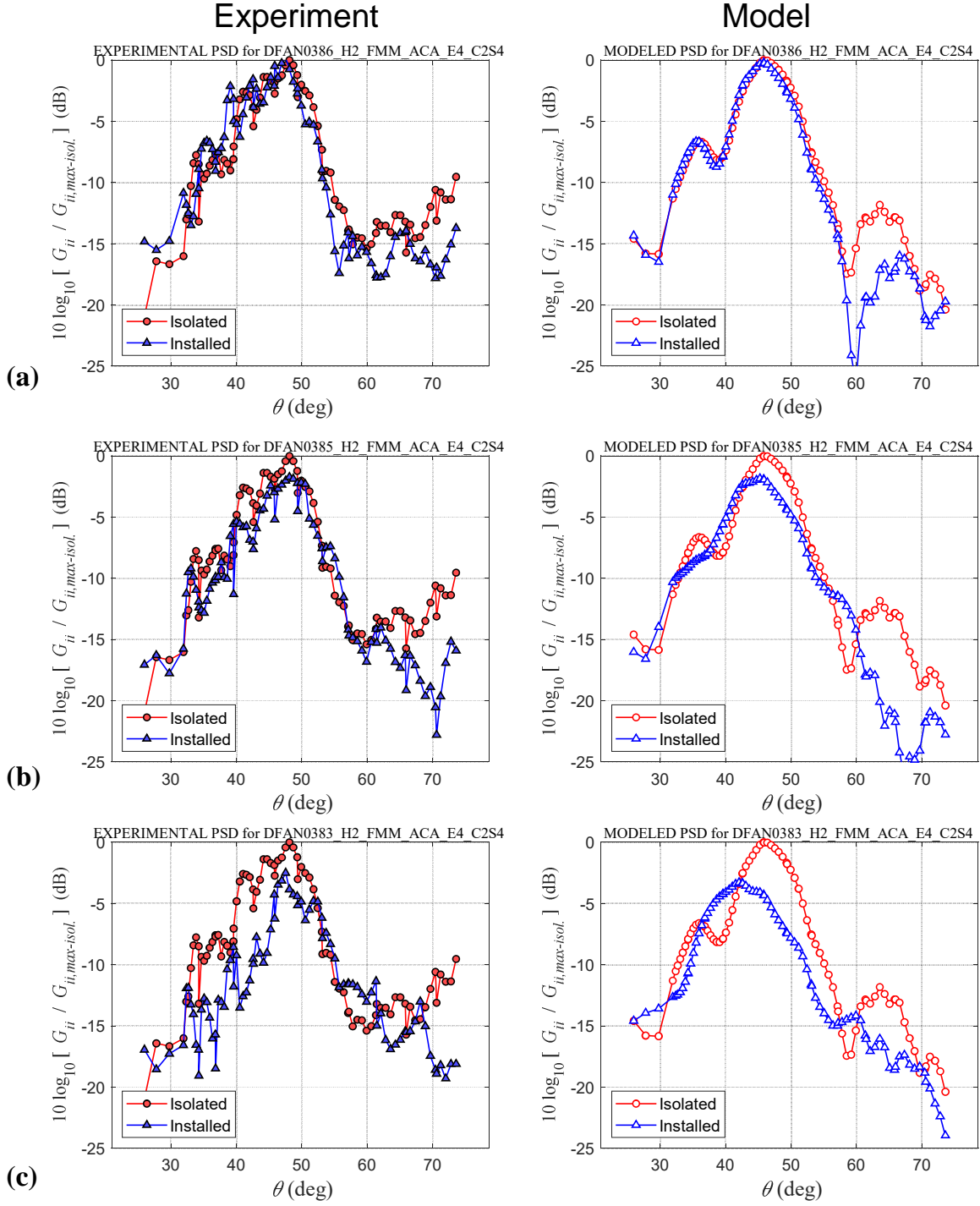
Fig. 14 **Experimental (left column) and modeled (right column) polar distributions of the isolated (red) and installed (blue) power spectral densities for $n_{\text{BPF}} = 2$. (a) X_{TE}=33 mm; (b) X_{TE}=55 mm; (c) (b) X_{TE}=78 mm.**
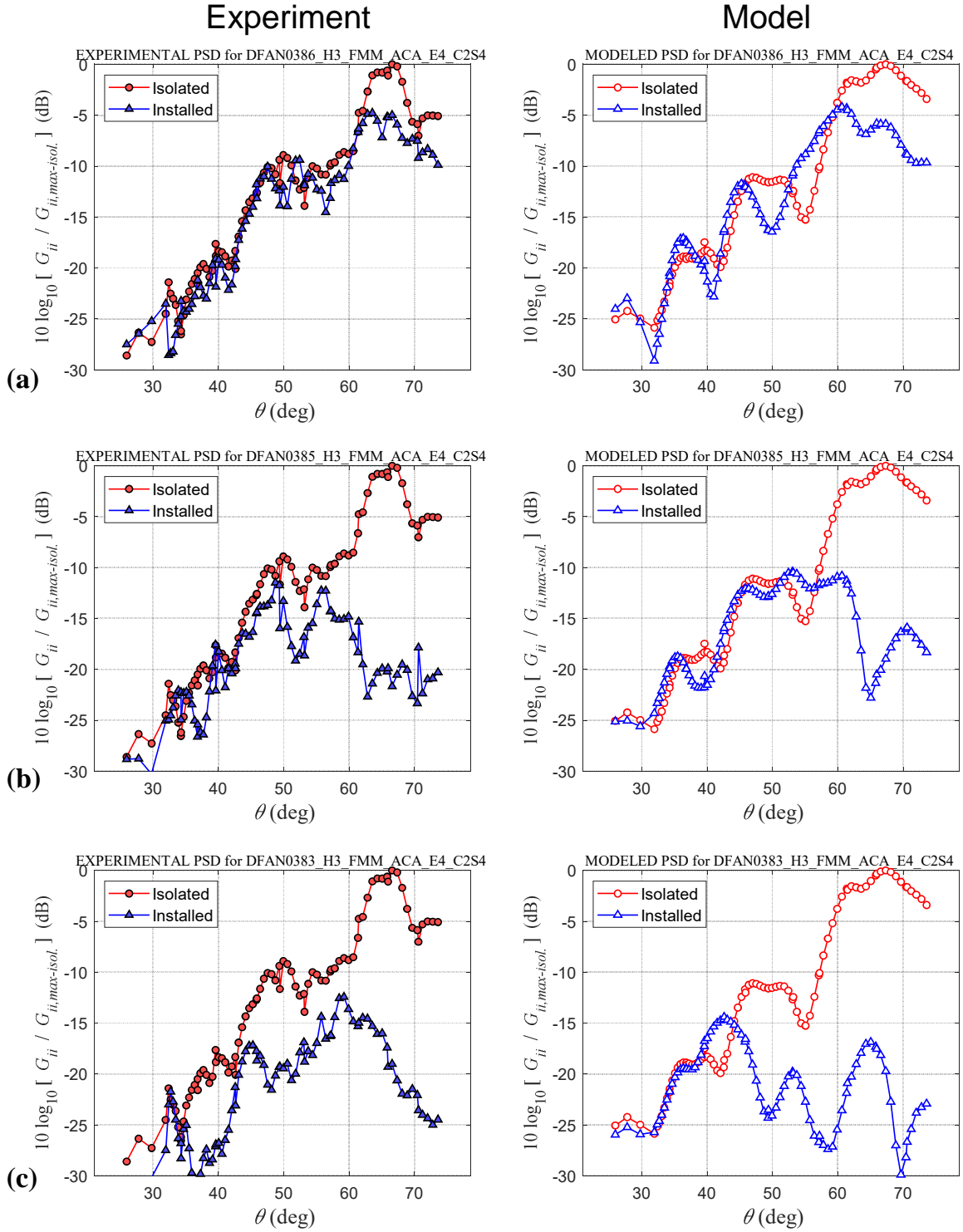
Fig. 15 **Experimental (left column) and modeled (right column) polar distributions of the isolated (red) and installed (blue) power spectral densities for $n_{\mathrm{BPF}} = 3$. (a) X_{TE}=33 mm; (b) X_{TE}=55 mm; (c) (b) X_{TE}=78 mm.**

16

V. Conclusions

The paper presented a coupled theoretical and experimental effort aimed at improving the fidelity of low-cost models of aft-emitted tonal fan noise in isolated and installed configurations. The source model is prescribed as linear waveforms on a cylindrical surface immediately following the fan duct with radius equal to that of the fan duct exit. The waveforms correspond to the aft-propagating cut-on modes in the duct and have azimuthal orders equal to those predicted by duct acoustics. The model for the axial evolution of the waveform was inspired by a theoretical treatment of diffraction from an annular aperture using the Kirchhoff approximation. This treatment indicated that the amplitude and convective Mach number of the waveform decay with axial distance.

In the modeling, the initial convective Mach number, at the duct exit, is maintained close to the value predicted by duct acoustics. The decay rate and initial amplitude of each waveform are included in a parameter vector that is determined by least-squares minimization of the difference between modeled and experimental cross-spectral densities in the far field. In installed arrangements, the emission from the parameterized source is used as the incident field for the prediction of scattering using the boundary element method.

The experiment used a small-scale ducted fan and microphone measurements with high spatial resolution enabled by the combination of fixed sensors with one scanning sensor. Harmonic-broadband separation utilized the Vold-Kalman filter, and the focus was placed on the second and third harmonics of the blade pass frequency. Integration of the ducted fan with a rectangular plate enabled measurements in a canonical shielded configuration. The results indicate a noise source with emission similar to Mach wave radiation from supersonic jets. The source becomes more compact with increasing frequency. The model captures the overall directivity of the experimental spectrum and its modification by insertion of the plate.

References

[1] Jones, S., Haller, W., and Tong, M., "An N+3 Technology Level Reference Propulsion System," *NASA/TM-2017-219501*, 2017.

[2] Spakovsky, Z., "Advanced Low-Noise Aircraft Configurations and their Assessment: Past, Present, and Future," *CEAS Aeronautical Journal*, Vol. 10, 2019, pp. 137–155. doi:10.1007/s13272-019-00371-8.

[3] Gerhold, C., Clark, L., Dunn, M., and Tweed, J., "Investigation of Acoustical Shielding by a Wedge-Shaped Airframe," *Journal of Sound and Vibration*, Vol. 294, No. 1-2, 2006, pp. 49–63. doi:10.1016/j.jsv.2005.10.010.

[4] Chappuis, J., Ricouard, J., and Roger, M., "Aft Fan Noise Shielding by a Lifting Surface: Analytical, Numerical, and Experimental Results," *AIAA Paper 2006-2617*, 2006. doi:10.2514/6.2006-2617.

[5] Thomas, R., Burley, C., and Olson, E., "Hybrid Wing Body Aircraft System Noise Assessment with Propulsion Airframe Aeroacoustic Experiments," *International Journal of Aeroacoustics*, Vol. 11, 2012. doi:10.1260/1475-472X.11.3-4.369.

[6] Berton, J., "Empennage Noise Shielding Benefits for an Open Rotor Transport," *AIAA Paper 2011-2764*, 2011. doi:10.2514/6.2011-2764.

[7] Liebeck, R., "Design of the Blended Wing Body Subsonic Transport," *Journal of Aircraft*, Vol. 41, No. 1, 2004, pp. 10–25. doi:10.2514/1.9084.

[8] Huang, X., Chen, Z., Ma, Z., and Zhang, X., "Efficient Computation of Spinning Modal Radiation Through an Engine Bypass Duct," *AIAA Journal*, Vol. 46, No. 6, 2008, pp. 1413–1423. doi:10.2514/1.31136.

[9] Redonnet, S., and Druon, Y., "Computational Aeroacoustics of Aft Fan Noise Characterizing a Realistic Coaxial Engine," *AIAA Journal*, Vol. 50, No. 5, 2012, pp. 1029–1046. doi:10.2514/1.J050730.

[10] Fernandes, L., Housman, J., Kenway, G., Stich, G.-T., and Kiris, C., "Fan Noise Predictions of the NASA Source Diagnostic Test using Unsteady Simulations with LAVA Part I: Near-Field Aerodynamics and Turbulence," *AIAA Paper 2023-0793*, 2023.

[11] Papamoschou, D., "Prediction of Jet Noise Shielding," *AIAA Paper 2010-0653*, 2010. doi:10.2514/6.2010-653.

[12] Mincu, D.-C., Manoha, E., Parzani, C., Chappuis, J., Redonnet, S., Davy, R., and Escouflair, M., "Numerical and Experimental Characterization of Aft-Fan Noise for Isolated and Installed Configurations," *AIAA Paper 2010-3918*, 2010. doi:10.2514/6.2010-3918.

[13] Nark, D., Burley, C., Tinetti, A., and Rawls, J., "Initial Integration of Noise Prediction Tools for Acoustic Scattering Effect," *AIAA Paper 2008-2996*, 2009. doi:10.2514/6.2008-2996.

[14] Papamoschou, D., "Modeling of Aft-Emitted Tonal Fan Noise in Isolated and Installed Configurations," *AIAA Paper 2021-0009*, 2021. doi:10.2514/6.2021-0009.

[15] Shah, P., Vold, H., Hensley, D., Envia, E., and Stephens, D., "A High-Resolution Continuous-Scan Acoustic Measurement Method for Turbofan Engine Applications," *Journal of Turbomachinery*, Vol. 137, 2015, pp. 121002–121002–11. doi:10.1115/1.4031341.

[16] Shah, P., Lee, A., Hensley, D., Schweizer, L., Yang, M., and Papamoschou, D., "Continuous-Scan Phased Array Measurement Methods for Turbofan Engine Acoustic Testing," *Journal of Engineering for Gas Turbines and Power*, Vol. 141, No. 8, 2019, pp. 081201–081201–13. doi:10.1115/1.4042395.

[17] Papamoschou, D., Morata, D., and Shah, P., "Inverse Acoustic Methodology for Continuous-Scan Phased Arrays," *AIAA Journal*, Vol. 57, No. 2, 2019, pp. 5126–5140. doi:10.2514/1.J058085.

[18] Truong, A., and Papamoschou, D., "Experimental Simulation of Ducted Fan Acoustics at Very Small Scale," *AIAA Paper 2014-0718*, 2014. doi:10.2514/6.2014-0718.

[19] Vold, H., and Leuridian, J., "High Resolution Order Tracking at Extreme Slew Rates Using Kalman Tracking Filters," *SAE Technical Paper 931288*, 1993. doi:10.4271/931288.

[20] Stephens, D., and Vold, H., "Order Tracking Signal Processing for Open Rotor Acoustics," *Journal of Sound and Vibration*, Vol. 333, 2014, pp. 3818–3830. doi:10.1016/j.jsv.2014.04.005.

[21] Truong, A., and Papamoschou, D., "Harmonic and Broadband Separation of Noise from a Small Ducted Fan," *AIAA Paper 2015-3282*, 2015. doi:10.2514/6.2015-3282.

[22] Papamoschou, D., "Imaging of Distributed Directional Noise Sources," *Journal of Sound and Vibration*, Vol. 330, No. 10, 2011, pp. 2265–2280. doi:10.1016/j.jsv.2010.11.025.

[23] Papamoschou, D., "Wavepacket Modeling of the Jet Noise Source," *International Journal of Aeroacoustics*, Vol. 17, No. 1-2, 2018, pp. 52–69. doi:10.1177/1475472X17743653.

[24] Tyler, J., and Sofrin, T., "Axial Flow Compressor Noise Studies," *SAE Transactions*, Vol. 70, 1962, pp. 309–332. doi:10.4271/620532.

[25] Savkar, S., "Radiation of Cylindrical Duct Acoustics Modes with Flow Mismatch," *Journal of Sound and Vibration*, Vol. 42, No. 3, 1975, pp. 363–386. doi:10.1016/0022-460X(75)90251-5.

[26] Rienstra, S., "Acoustic Radiation from a Semi-Infinite Annular Duct in a Uniform Subsonic Mean Flow," *Journal of Sound and Vibration*, Vol. 94, No. 2, 1984, pp. 267–288. doi:10.1016/S0022-460X(84)80036-X.

[27] Eversman, W., "Aft Fan Duct Acoustic Radiation," *Journal of Sound and Vibration*, Vol. 213, No. 2, 1998, pp. 235–257. doi:10.1006/jsvi.1997.1480.

[28] Redonnet, S., Desquenes, G., and Manoha, E., "Numerical Study of Acoustic Installation Effects with a Computational Aeroacoustics Methods," *AIAA Journal*, Vol. 48, No. 5, 2010, pp. 1029–1046. doi:10.2514/1.42153.

[29] Rice, E., and Saule, A., "Far-Field Radiation of Aft Turbofan Noise," *NASA TM 81506*, 1980.

[30] Saule, A., "Modal Structure Inferred from Static Far-Field Noise Directivity," *AIAA Paper 1976-0574*, 1976.

[31] Rice, E., "Multimodal Far-Field Acoustics Radiation Pattern Using Mode Cutoff Ratio," *AIAA Journal*, Vol. 16, No. 9, 1978, pp. 1029–1046. doi:10.2514/3.60984.

[32] Keller, J., Lewis, R., and Bernard, D., "Diffraction by an Aperture. II," *Journal of Applied Physics*, Vol. 28, No. 5, 1957, pp. 570–579. doi:10.1063/1.1722805.

[33] Shanno, D. F., and Phua, K. H., "Minimization of Unconstrained Multivariate Functions," *ACM Transactions on Mathematical Software*, Vol. 6, No. 4, 1976, pp. 618–622. doi:10.1145/355666.355673.

[34] Liu, Y., "Fast Multipole Boundary Element Method: Theory and Applications in Engineering," Cambridge University Press, Cambridge, 2009. doi:10.1017/CBO9780511605345.